ACS Catalysis

Research Article

Cite This: ACS Catal. 2018, 8, 2218–2224

pubs.acs.org/acscatalysis

Ab Initio Simulation Explains the Enhancement of Catalytic Oxygen Evolution on $CaMnO_3$

Tian Qiu,[†] Bingtian Tu,[‡] Diomedes Saldana-Greco,[†] and Andrew M. Rappe*[,†]

[†]Department of Chemistry, University of Pennsylvania, Philadelphia, Pennsylvania 19104-6323, United States

[‡]State Key Lab of Advanced Technology for Materials Synthesis and Processing, Wuhan University of Technology, Wuhan, People's Republic of China

ABSTRACT: Experimental results have shown promising catalytic activity for the oxygen evolution reaction (OER) on the perovskite-type material $CaMnO_3$. Through density functional theory investigations, we study the OER mechanism on $CaMnO_3$, on the basis of a thermodynamic stability approach. Our results reveal that the formation of Mn vacancies caused by the solubility of Mn enhances lattice oxygen activity, which then reduces the energy of the adsorbate *OOH and therefore loosens the lower overpotential limit predicted from the "scaling relationship". This effect suggests that, by doping manganite oxides with soluble elements, we could enhance their OER catalytic activities due to the high surface lattice oxygen activity induced by surface metal ion vacancies.

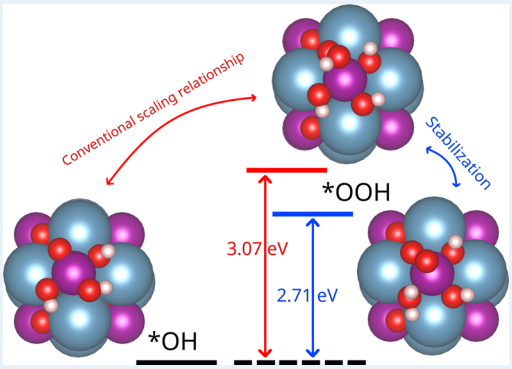

KEYWORDS: *electrocatalysis, oxygen evolution, calcium manganite, density functional theory, aqueous surface phase diagram*

INTRODUCTION

The scarcity of nonrenewable fossil fuels, along with the increasing demand for energy, has attracted significant attention to the development of sources of alternative and renewable energy. One of the most promising alternatives is the field of electrochemical energy conversion, such as fuel cells, metal–air batteries, and electrolysis. It is clear that reducing the energy loss of the oxygen evolution reaction (OER) and the oxygen reduction reaction (ORR) is vital in enhancing overall electrochemical energy conversion efficiency. For the electrolysis of water, IrO_2 and RuO_2 have been reported as promising electrocatalysts due to their high activity for the OER.[1−3] However, since these materials are rare and expensive, current research is focused on searching for inexpensive alternative materials with comparable or even higher catalytic activity. Manganese compounds have shown significant advantages in this competition. Their high abundance and relatively low price ensure their availability for large-scale energy conversion. Studies of the Mn_4O_4 cubane show its crucial role in photosynthesis,[4] and recent work shows that nanostructured α-Mn_2O_3 is an excellent bifunctional catalyst for the OER and ORR.[5] Perovskites with $Mn^{3+/4+}$ as B-site cations also exhibit impressive catalysis activity. Du et al.[6] and Kim et al.[7] have found that the required OER potential on $CaMnO_{3-x}$ decreases from $U_{RHE} \approx 1.6$ V to $U_{RHE} \approx 1.5$ V when x increases from 0 to 0.25, where x stands for vacancy cocentration, RHE stands for "reversible hydrogen electrode", and U_{RHE} stands for electrode potential referenced to the RHE. Noting that the required OER potential on IrO_2 is also 1.5 V, this suggests that manganites can provide the highest level of OER catalysis activity. However, to our knowledge, there is no systematic theoretical work investigating the OER process on $CaMnO_3$. In order to make further development in the design of new materials, a thorough understanding of the catalytic mechanism is required.

Previous work has shown that there are at least two types of OER mechanisms:[8−10] namely the adsorbate–evolution mechanism (AEM) and the Mars–van Krevelen type mechanism (MKM). In a common AEM, oxygen is evolved at one active site on the surface through the intermediates of *OH, *O, and *OOH and then is released as O_2. In MKM, the lattice oxygen can directly participate in the formation of O_2, and in some cases two cooperative sites could be involved in the formation of a single O_2 molecule. Since surfaces of perovskite-type materials may undergo reconstructions in an aqueous environment,[11] multiple local geometries at the active site could be expected on different materials or under different conditions. Therefore, exploring the OER mechanism on reconstructed perovskite-type materials may disclose new features that provide novel opportunities for enhanced catalysis.

The required electrode potential for the OER is the minimal voltage under which all four steps of intermediate evolution are spontaneous. Knowing that the Gibbs free energy change of the total oxygen evolution reaction $2H_2O \rightarrow 4H^+ + 4e^- + O_2$ is independent of the reaction path, the required electrode potential reaches its minimum (U_{RHE} = 1.23 V) if four

Received: November 22, 2017
Revised: January 29, 2018
Published: January 31, 2018

DOI: 10.1021/acscatal.7b03987
ACS Catal. 2018, 8, 2218–2224

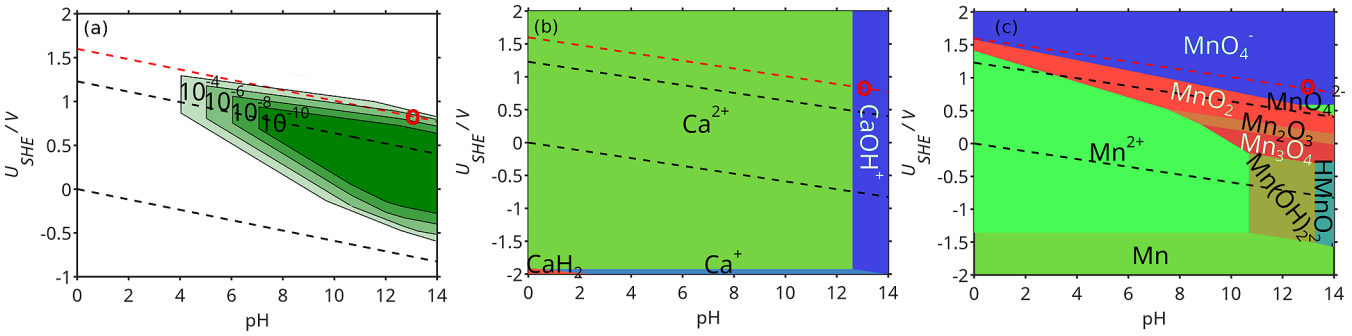

Figure 1. (a) Bulk stability region of $CaMnO_3$ under different concentrations of aqueous species. All concentrations are in units of mol/L (abbreviated M). The red dashed line is U_{RHE} = 1.6 eV, and the red circle labels the experimental conditions under which the OER has been conducted on $CaMnO_3$.[7] The black dashed lines are (upper) O_2/H_2O equilibrium line and (lower) H_2/H_2O equilibrium line. (b) Pourbaix diagram, showing the most stable aqueous forms of Ca with a concentration of 10^{-6} M. (c) Pourbaix diagram, showing the most stable aqueous forms of Mn with a concentration of 10^{-6} M.

intermediates are evenly spaced on the free energy scale: i.e., all four single-electron-transfer reactions have the same reaction free energy. Any deviation from the evenly spaced case causes at least one single-electron-transfer reaction to have higher reaction free energy in comparison to the average and therefore requires extra electrode potential referring as "overpotential" (η) to be spontaneous.[9,12,13] η is directly related to energy losses during the electrochemical reaction. Recent theoretical studies of AEM have stated that the adsorption energy difference between *OOH and *OH is approximately 3.2 eV regardless of metal ion identity at the active site.[9] A direct conclusion from this "scaling relationship" is that there would be a lower limit for η: $\eta \geqslant (3.2/2) - 1.23 = 0.37$ (eV). However, since surfaces of perovskite-type materials can undergo reconstructions, it is possible that the local chemical environment at the active site on the surface influences *OH and *OOH in a different way such that this scaling relationship may not apply.

Since the thermodynamically stable (oxy)hydroxides are the most relevant structures in the OER,[10,14] we follow the thermodynamic-stability-based approach to study the OER mechanism on the perovskite-type material $CaMnO_3$. The adsorbates could still be identified as *OH, *O, and *OOH on different surface sites to some extent, but the high activity of the lattice oxygens makes them able to host hydrogen atoms as well as interact with protons from the adsorbates. We notice that the proton from *OOH has a strong interaction with the lattice oxygen and even transfers to the lattice oxygen site, while the proton from *OH is less active and could not be further stabilized by transferring to the lattice oxygen site. Since this process lowers the energy of *OOH, and consequently reduces the adsorption energy difference between *OOH and *OH, it may guide the design of catalysts with lower overpotential for the OER.

METHODS AND RESULTS

Prior to the investigation of the OER mechanism, the bulk stability region of $CaMnO_3$ in an aqueous environment must be evaluated in order to estimate the concentrations of aqueous ions involved in further simulations. The scheme for computing the bulk stability region is well established,[11] based on finding the pH-U region such that the following reaction is spontaneous:

$$\sum_{A} n_A H_x AO_y^{z-} \rightarrow CaMnO_3 + n_{H_2O} H_2O + n_{H^+} H^+ + n_e e^- \quad (1)$$

where the sum accounts for all elements "A" in the bulk and n_A, n_{H_2O}, n_{H^+}, and n_e stand for the numbers of A elements, H_2O, H^+, and e^- involved in the reaction, respectively. $H_xAO_y^{z-}$ is the most thermodynamically stable aqueous form of "A" at a given pH and U. Its exact form is determined by selecting the species with the lowest formation energy, according to the equation

$$A + n_{H_2O} H_2O \rightarrow H_x AO_y^{z-} + n_{H^+} H^+ + n_e e^- \quad (2)$$

The result is usually plotted as a Pourbaix diagram[11,15] (Figure 1). If we note that under experimental conditions U_{RHE} = 1.6 eV and pH 13,[7] the concentration of aqueous species is approximately 10^{-6} M. This value is used in the rest of the calculations.

The stability of surfaces in an aqueous environment must be evaluated considering the interaction between surfaces and the solvent.[10,11] A rigorous consideration of surface evolution should include both metal ion exchange and hydration/(de)hydrogenation. However, since the complex metal ion exchange process is less likely to be involved in the OER cycle, we could first consider metal ion exchange and the associated oxygen exchange and then investigate the hydration and (de)hydrogenation process to construct OER cycles on each of the surfaces with different surface metal ion concentrations and finally rule out catalytic cycles that require electrode potential beyond their surface stability region.

The comparison of surface stability during the metal ion exchange step can be conducted by establishing the following reaction between surfaces:

$$R_i + n_{H_2O} H_2O \rightarrow R_j + \sum_{A} n_A H_x AO_y^{z-} + n_{H^+} H^+ + n_e e^- \quad \Delta G \quad (3)$$

where R_i and R_j are different surface reconstructions. The sum accounts for all elements "A" that are exchanged between the surface and the solvent. Since this reaction describes the transformation between different surfaces, the reaction free energy (ΔG) can be treated as the "relative formation energy" of each surface (R_j) if one surface R_i is assigned as the reference surface (R_{ref}). Under this definition, the surface with the most negative relative formation energy is the most stable surface

DOI: 10.1021/acscatal.7b03987
ACS Catal. 2018, 8, 2218−2224

under given pH and electrode potential U. A Hess's law related approach proposed by Rong et al. is selected to calculate ΔG:[11]

$$\mathrm{R}_{\mathrm{ref}} \rightarrow \sum_{\mathrm{A}} n_{\mathrm{A}}\mathrm{A} + \mathrm{R}_j \quad \Delta G_1$$

$$\sum_{\mathrm{A}} n_{\mathrm{A}}\mathrm{A} + n_{\mathrm{H_2O}}\mathrm{H_2O} \rightarrow \sum_{\mathrm{A}} n_{\mathrm{A}}\mathrm{H}_x\mathrm{AO}_y^{z-} + n_{\mathrm{H^+}}\mathrm{H^+} + n_{\mathrm{e}}\mathrm{e^-} \quad \Delta G_2$$

$$\Delta G = \Delta G_1 + \Delta G_2$$

ΔG_1 can be calculated from density functional theory (DFT), and ΔG_2 can be evaluated from experimental thermodynamic data of free energy per A at standard state relative to the standard hydrogen electrode (SHE), $\Delta G^\circ_{\mathrm{A,SHE}}$:

$$\begin{aligned}
\Delta G_1 &= \left(\Delta H_j + \sum_{\mathrm{A}} n_{\mathrm{A}}\Delta H_{\mathrm{A}} - \Delta H_{\mathrm{ref}}\right) - T\left(\Delta S_j + \sum_{\mathrm{A}} n_{\mathrm{A}}\Delta S_{\mathrm{A}} - \Delta S_{\mathrm{ref}}\right) \\
&\approx \left(\Delta E_j + \sum_{\mathrm{A}} n_{\mathrm{A}}\Delta E_{\mathrm{A}} - \Delta E_{\mathrm{ref}}\right) - T\sum_{\mathrm{A}} n_{\mathrm{A}}\Delta S_{\mathrm{A}} \\
\Delta G_2 &= \sum_{\mathrm{A}} n_{\mathrm{A}}(\mu^\circ_{\mathrm{H}_x\mathrm{AO}_y^{z-}} - \mu^\circ_{\mathrm{A}}) + n_{\mathrm{H^+}}\mu^\circ_{\mathrm{H^+}} + n_{\mathrm{e}}\mu^\circ_{\mathrm{e}} - n_{\mathrm{H_2O}}\mu^\circ_{\mathrm{H_2O}} + \\
&\quad \sum_{\mathrm{A}} kT\ln a_{\mathrm{H}_x\mathrm{AO}_y^{z-}} - 2.3n_{\mathrm{H^+}}kT\mathrm{pH} + n_{\mathrm{e}}eU_{\mathrm{SHE}} \\
&= \sum_{\mathrm{A}} \Delta G^\circ_{\mathrm{H}_x\mathrm{AO}_y^{z-},\mathrm{SHE}} + \sum_{\mathrm{A}} kT\ln a_{\mathrm{H}_x\mathrm{AO}_y^{z-}} - 2.3n_{\mathrm{H^+}}kT\mathrm{pH} + n_{\mathrm{e}}eU_{\mathrm{SHE}}
\end{aligned} \tag{4}$$

where the entropy differences between surfaces are neglected.[16] Next, to study the hydration and (de)hydrogenation processes on surfaces, the relative thermodynamic stability at a given pH and U can be established through the reaction free energy $\Delta\tilde{G}_k$ of the following reaction for each hydration and (de)-hydrogenation state k:

$$\tilde{\mathrm{R}}_{\mathrm{ref}} + n_{\mathrm{H_2O}}\mathrm{H_2O} \rightarrow \tilde{\mathrm{R}}_k + n_{\mathrm{H^+}}(\mathrm{H^+} + \mathrm{e^-}) \quad \Delta\tilde{G}_k \tag{5}$$

where the most stable surface predicted from the metal-ion exchange step can be chosen as $\tilde{\mathrm{R}}_{\mathrm{ref}}$.

The number of electrons (or protons) that are released in this reaction can be treated as a label n_k of the state $\tilde{\mathrm{R}}_k$ on an oxidization ladder. Knowing that it is always possible to write OER as a sequence of four single-electron transfer reactions:

$$\tilde{\mathrm{R}}_0 \xrightarrow[(+\mathrm{H_2O})-\mathrm{H^+}]{-\mathrm{e^-}} \tilde{\mathrm{R}}_1 \xrightarrow[(+\mathrm{H_2O})-\mathrm{H^+}]{-\mathrm{e^-}} \tilde{\mathrm{R}}_2 \xrightarrow[(+\mathrm{H_2O})-\mathrm{H^+}]{-\mathrm{e^-}} \tilde{\mathrm{R}}_3 \xrightarrow[(+\mathrm{H_2O})-\mathrm{H^+}]{-\mathrm{e^-}} \tilde{\mathrm{R}}_0 + \mathrm{O_2}$$

in which two H_2O molecules (or OH^-) are included at certain steps and the label n_k of each state $\tilde{\mathrm{R}}_k$ is increased by 1 successively from $\tilde{\mathrm{R}}_0$ to $\tilde{\mathrm{R}}_3$, due to the removal of an electron at each step. With this relationship, the OER path can be naturally determined instead of being arbitrarily selected. To determine the OER path, notice that all four reactions must be made spontaneous by applying the required electrode potential: i.e. $\Delta\tilde{G}_0 \geqslant \Delta\tilde{G}_1 \geqslant \Delta\tilde{G}_2 \geqslant \Delta\tilde{G}_3 \geqslant \Delta\tilde{G}_0 - 4e(U - \phi^\circ_{\mathrm{O_2/H_2O}})$ at a pH and U, it can be immediately concluded that the state $\tilde{\mathrm{R}}_k$ with the lowest $\Delta\tilde{G}_k$ at a pH and U takes the place of $\tilde{\mathrm{R}}_3$ in the OER cycle. Once $\tilde{\mathrm{R}}_3$ is determined, the labels n_k of the other three intermediates are automatically determined, and therefore the identity of each of them can be determined by selecting the most thermodynamically stable surface with the correct label n_k for this OER step.

The structure and energetics of $CaMnO_3$ with different surface reconstructions are computed with first-principles DFT using the Perdew–Burke–Ernzerhof functional revised for solids (PBEsol)[17] as implemented in the QUANTUM ESPRESSO package.[18] The calculations account for spin-polarized electronic densities. All atoms are represented by norm-conserving, optimized,[19] designed nonlocal[20] pseudopotentials generated with the OPIUM package,[21] treating 2s and 2p of O, 3s, 3p, 3d, and 4s of Ca, and 3s, 3p, 3d, 4s, and 4p of Mn as semicore and valence states. In addition to the inclusion of semicore states, the Mn pseudopotential also includes nonlinear core–valence interaction via the partial core correction scheme.[22−24] A rotationally invariant DFT+U+J scheme[25] is applied for Mn. U_{eff} = 1.6 V is chosen from ref 26, and J_0 = 1.08 V is calculated from the linear response method.[25,27] All calculations are performed with a 70 Ry plane-wave energy cutoff.[26] The Brillouin zone is sampled using 4 × 4 × 1 Monkhorst–Pack[28] k-point meshes for the slab calculations. The $\sqrt{2} \times \sqrt{2}$ $R45°$ nine-layer supercell is chosen for all surface configurations. Surface adsorbates and bare surface structures are relaxed with 13 Å vacuum and a dipole correction[29] to cancel the artificial interaction between the system and its periodic images.

MnO_2-terminated (001) surfaces and CaO-terminated (001) surfaces with various O adatoms, O vacancies, Mn vacancies, and Ca vacancies are considered. A subset of the involved surfaces is shown in Figure 2. The most stable surface

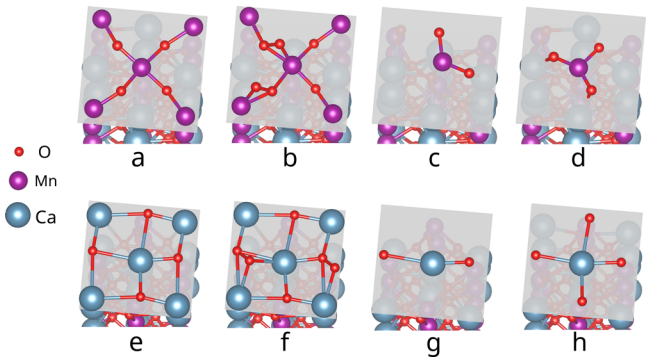

Figure 2. Examples of relaxed surfaces with different numbers of adsorbates and vacancies: (a) Mn_2O_4; (b) Mn_2O_4 + 2.0O; (c) Mn_2O_4 − 1.0Mn − 2.0O; (d) Mn_2O_4 − 1.0Mn − 1.0O; (e) Ca_2O_2; (f) Ca_2O_2 + 1.0O; (g) Ca_2O_2 − 1.0Ca − 1.0O; (h) Ca_2O_2 − 1.0Ca.

reconstructions are reported as a phase diagram in Figure 3a. Surfaces are named with the format "termination ± #atom", where + and − represent adatoms and vacancies, respectively, and # represents the number of atoms introduced/removed per supercell relative to a reference surface with fixed termination, which can be either Mn_2O_4 or Ca_2O_2. Figure 3a shows that there are two surface reconstructions whose stability regions extend above the O_2/H_2O equilibrium line: namely, Mn_2O_4 +

DOI: 10.1021/acscatal.7b03987
ACS Catal. 2018, 8, 2218−2224

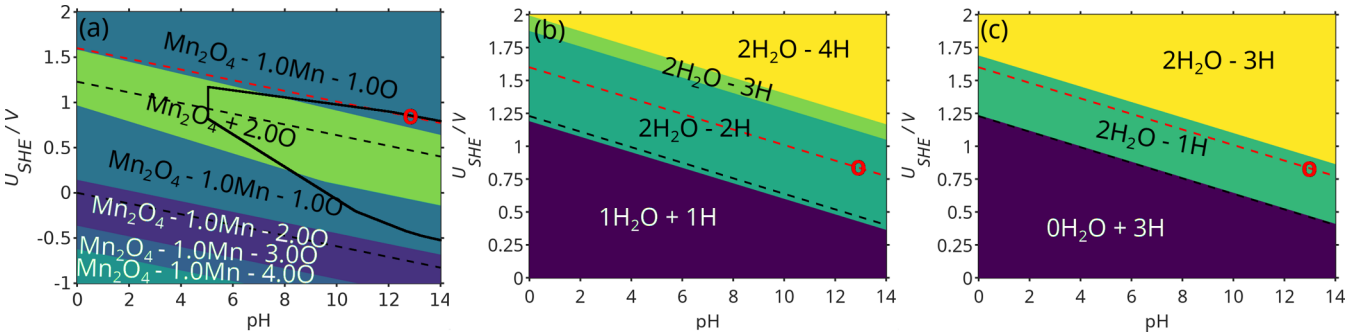

Figure 3. (a) Phase diagram of the most stable surface reconstruction. The solid black line represents the bulk stability region of $CaMnO_3$ with the concentration of aqueous species being 10^{-6} M. The two disjoint regions for the same surface Mn_2O_4 − 1.0Mn − 1.0O should relate to changes in solubility of the Mn ion when the electrode potential is increased. (b) Phase diagram of the most stable hydration and (de)hydrogenation states of surface Mn_2O_4 + 2.0O. (c) Phase diagram of the most stable hydration and (de)hydrogenation states of surface Mn_2O_4 − 1.0Mn − 1.0O.

2.0O and Mn_2O_4 − 1.0Mn − 1.0O. Hence, the hydration and (de)hydrogenation process are evaluated on both surfaces.

By application of the scheme mentioned in eq 5, results of the most stable hydration and oxidation states are shown in Figure 3b,c. Conditions are named with the format "#H_2O ± #H", where # is the number of H_2O and H introduced to or removed from the surface per supercell. For the case of Mn_2O_4 − 1.0Mn − 1.0O, since $2H_2O$ − 1H is in the stability region at or above the O_2/H_2O equilibrium line, we first assume this state to be the intermediate $\tilde{R}_3$ in the OER cycle on surface Mn_2O_4 − 1.0Mn − 1.0O. Since the position on the oxidization ladder is only determined by "±#H", $\tilde{R}_0$, $\tilde{R}_1$, and $\tilde{R}_2$ should take the form of #H_2O + 2H, #H_2O + 1H, and #H_2O + 0H, respectively, and their exact identities are given in Table 1.

Table 1. Identities of Intermediates

Mn_2O_4 − 1.0Mn − 1.0O		Mn_2O_4 + 2.0O	
intermediate	identity	intermediate	identity
$\tilde{R}_0$	+1H_2O + 2H	$\tilde{R}'_0$	+1H_2O + 1H
$\tilde{R}_1$	+1H_2O + 1H	$\tilde{R}'_1$	+1H_2O + 0H
$\tilde{R}_2$	+2H_2O + 0H	$\tilde{R}'_2$	+2H_2O − 1H
$\tilde{R}_3$	+2H_2O − 1H	$\tilde{R}'_3$	+2H_2O − 2H

Intermediates $\tilde{R}_k$ and $\tilde{R}'_k$ are built up from different surface reconstructions listed in the first row. Once the OER cycle is determined, the required electrode potential could be calculated accordingly. For this reaction cycle on the Mn_2O_4 − 1.0Mn − 1.0O surface, the required electrode potential is U_{RHE} = 1.62 V, as can be found in Table 2. This potential is

Table 2. Reaction Free Energy for Each Step in the OER

Mn_2O_4 − 1.0Mn − 1.0O		Mn_2O_4 + 2.0O	
reaction step	ΔG_{RHE}/eV	reaction step	ΔG_{RHE}/eV
(1) $\tilde{R}_0 \rightarrow \tilde{R}_1$	1.62	(1) $\tilde{R}'_0 \rightarrow \tilde{R}'_1$	1.90
(2) $\tilde{R}_1 \rightarrow \tilde{R}_2$	1.09	(2) $\tilde{R}'_1 \rightarrow \tilde{R}'_2$	1.23
(3) $\tilde{R}_2 \rightarrow \tilde{R}_3$	0.82	(3) $\tilde{R}'_2 \rightarrow \tilde{R}'_3$	0.44
(4) $\tilde{R}_3 \rightarrow \tilde{R}_0 + O_2$	1.39	(4) $\tilde{R}'_3 \rightarrow \tilde{R}'_0 + O_2$	1.35

consistent with the stability region of metal ion exchange and surface hydration and (de)hydrogenation, certifying the OER cycle on this surface reconstruction. If the surface were not stable at the computed overpotential, the most stable hydration and (de)hydrogenation phase in a higher potential region would need to be assigned as $\tilde{R}_3$ and the process of constructing the OER cycle repeated. The same procedure is applied for the case of Mn_2O_4 + 2.0O, and the corresponding results are given in Tables 1 and 2. It can be noticed that the required OER electrode potential on the Mn_2O_4 + 2.0O surface (U_{RHE} = 1.90 V) is out of its ion exchange stability region, and so it is ruled out. Therefore, we predict that the oxygen evolves at the Mn site on the Mn_2O_4 − 1.0Mn − 1.0O surface. The computed electrode potential is U_{RHE} = 1.62 eV, which is in great agreement with the experimental value, U_{RHE} = 1.6 eV.[7]

The OER mechanisms are shown in Figure 4. Although we predict that Mn_2O_4 − 1.0Mn − 1.0O is the surface involved in the reaction, it is worthwhile to discuss and compare the OER mechanism on both surfaces. For the case of Mn_2O_4 − 1.0Mn − 1.0O, OER starts with the state that all four oxygen atoms are hydrogenated. At reaction step 1, one proton and electron are removed from an oxygen. Then, in step 2, an OH is attached to the surface, with the hydroxyl oxygen bonding to the deprotonated surface oxygen and the proton transferring to a hydrogenated surface oxygen. The transferred proton creates an H_2O molecule at a lattice oxygen site. At reaction step 3, the transferred proton and one electron are removed, turning the H_2O into surface OH. At step 4, an OH^- group from the solvent kicks off the O_2 and occupies the lattice oxygen site, with the removal of one electron. This reaction mechanism is very similar to that in Figure 4c in ref 30. Since the lattice oxygen is involved in the generation of O_2, the whole process should be classified as an MKM process. If this reaction cycle is compared with the most commonly studied AEM, it is possible to establish similarities in adsorbates, as well as differences in three aspects: the H from *OOH transfers to the lattice oxygen, OO does not leave the surface after the oxidization (at step 3) of *OOH, but stays on the surface as a superoxide, and adsorbates evolve at the lattice oxygen vacancy rather than on top of the metal ion.

The OER cycle on the Mn_2O_4 + 2.0O surface starts with *OH adsorbed on one Mn and two of the lattice oxygen atoms hydrogenated. At reaction step 1, the hydrogen from one of the lattice oxygens (not the adsorbed hydroxy) is removed. Then, at step 2, OH^- from the solvent interacts with the adsorbed *OH, transferring one proton to the lattice oxygen and forming *OOH, with one electron released. At step 3, the proton from the *OOH is removed, associated with the removal of one electron. Finally at step 4, O_2 is released and *OH adsorbs at the active site, restoring the surface to its initial state.

It can be noticed that $\tilde{R}'_0$ and $\tilde{R}'_2$ in the OER cycle on the Mn_2O_4 + 2.0O surface are analogues of *OH and *OOH in

DOI: 10.1021/acscatal.7b03987
ACS Catal. 2018, 8, 2218−2224

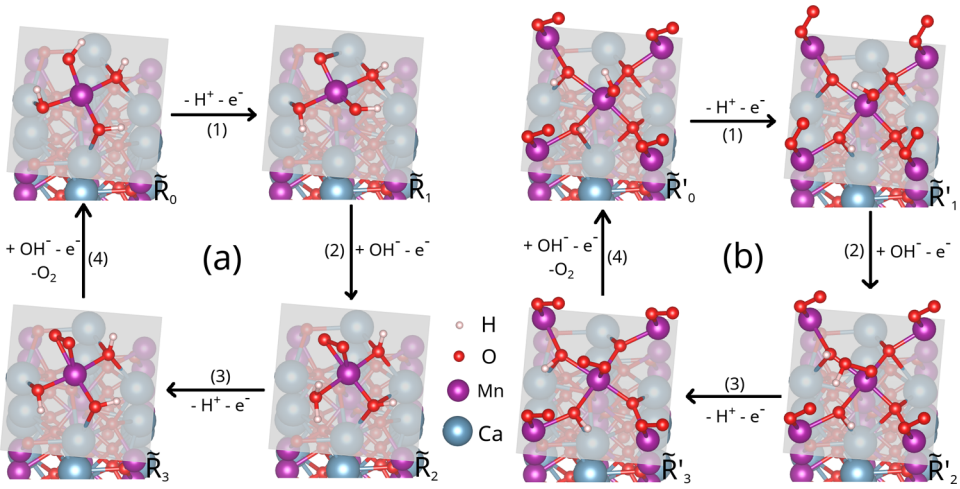

Figure 4. (a) OER cycle on surface Mn_2O_4 − 1.0Mn − 1.0O. (b) OER cycle on surface Mn_2O_4 + 2.0O.

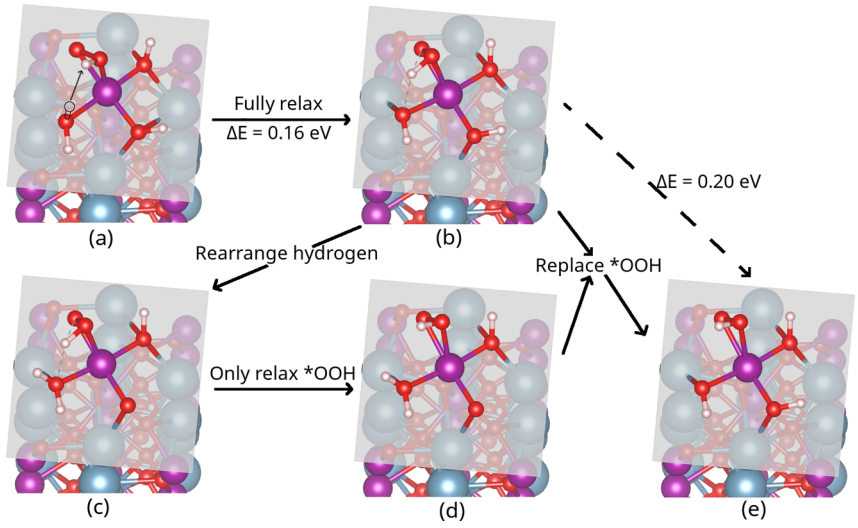

Figure 5. Investigation of the lattice oxygen−hydrogen interaction: (a) geometry of moving the hydrogen from the lattice oxygen to the O_2 adsorbate before relaxation; (b) strong interaction still existing between the lattice oxygen and the hydrogen; (c, d) screening of the attraction between the lattice oxygen and the hydrogen; (e) geometry of the intermediate $\tilde{R}_2$ if the lattice oxygen−hydrogen interaction is neglected. In all, H transfer to lattice O stabilizes this state by at least 0.36 eV, providing a way to break the conventional OH−OOH scaling relationship.

AEM. The free energy difference between these two intermediates can be calculated using the reaction free energy given in Table 2. The result $\Delta\tilde{G}'_2 - \Delta\tilde{G}'_0$ = 1.90 eV + 1.23 eV = 3.13 eV (referenced to the RHE) is close to the proposed value (3.2 eV) in the "scaling relationship". The OER process on the Mn_2O_4 − 1.0Mn − 1.0O surface is different from what is described in the AEM as mentioned above, but it is still possible to identify the *OH, *O, and $*O_2$ in $\tilde{R}_0$, $\tilde{R}_1$, and $\tilde{R}_3$, respectively, as they all occupy the same site. The adsorbate at the active site in $\tilde{R}_2$ is different from *OOH, but we can treat it as *OOH with the proton transferred to the lattice oxygen site and investigate the influence of this proton transfer phenomenon. Adding up the reaction free energy of steps 1 and 2 shows that the free energy difference between $\tilde{R}_0$ and $\tilde{R}_2$ is 1.62 eV + 1.09 eV = 2.71 eV. This value is notably smaller than the expected free energy difference between *OOH and *OH (3.2 eV), suggesting the violation of the "scaling relationship". In order to confirm whether the violation is caused by the proton transfer, we move the hydrogen back to the adsorbed oxygen site (Figure 5a) and let the structure relax (Figure 5b). The energy is increased by 0.16 eV, but there is still strong interaction between the lattice oxygen and the proton. In order to eliminate this interaction, we first let the lattice oxygen bond with another hydrogen atom pointing away from *OOH, remove one hydrogen atom from one lattice oxygen, and only allow the three atoms in *OOH to relax, as shown in Figure 5c,d. Then, we replace the *OOH in Figure 5b with the relaxed group in Figure 5d to achieve the final geometry (see Figure 5e) and perform the scf calculation for this geometry. From Figure 5b to Figure 5e, the energy is further increased by 0.20 eV, meaning that the lattice oxygen−hydrogen interaction reduces the energy by approximately 0.36 eV in total. This suggests that the proton transfer process indeed makes a significant contribution to the weakening of the "scaling relationship".

The lattice oxygen hydrogen-transfer process is driven by the strong activity of the lattice oxygen, which itself could be attributed to the formation of Mn vacancies. Surface atoms are less coordinated, in comparison with atoms in the bulk, and the dissolution of Mn ions further reduces the coordination number of the neighboring lattice oxygen atoms. In order to compensate for the missing lattice Mn, lattice oxygen interacts

DOI: 10.1021/acscatal.7b03987
ACS Catal. 2018, 8, 2218−2224

with the hydrogen atoms, as can be seen by noting the contrast (Figure 4) that half of the surface lattice oxygens are hydrogenated in $\tilde{R}'_0$, while all surface lattice oxygen atoms are hydrogenated in $\tilde{R}_0$, the surface with Mn vacancies. It is also worthwhile to consider whether or not hydrogen transfer occurs between *OH and lattice oxygen. An examination of Figure 4a and Table 2 shows that reaction 1 has 0.8 eV higher reaction free energy than reaction 3. This difference would be even larger if the hydrogen were bonded to *OO to make it *OOH in $\tilde{R}_2$, since it would make $\tilde{R}_2$ less stable. Although the over 0.8 eV reaction free energy difference could not be fully attributed to differences in O−H bond strength between *OH and *OOH, it still shows that the hydrogen from *OH is much less likely to transfer to the lattice oxygen, in comparison with the hydrogen in *OOH.

The enhanced activity of lattice oxygen also induces the formation of the MnO_2 triatomic ring as the intermediate of O_2 formation, rather than *OOH standing on the surface, which could be another factor leading to a reduced energy difference between *OH and *OOH. If we trace back further for the reason for Mn vacancy formation, the high solubility of MnO_4^- ion plays the role. Following this analysis, we suggest that doping the B-site element with a more soluble element could be a possible way to reduce the overpotential for the OER process on perovskite-type materials. It is constructive to compare our conclusion with the work in ref 31, where A-site cation deficiency in the perovskite-type materal $LaFeO_3$ enhances the OER and ORR performance. The researchers attribute the improvement to the formation of lattice oxygen vacancies on the surface induced by A-site vacancies. Our claim, however, is based on the enhanced activity of lattice oxygen atoms surrounding the metal ion vacancies that do not directly participate in the formation of oxygen molecules. Since these lattice oxygen atoms need to bond to active metal ions as well, it requires the substitution of active metal ions at the B site. In addition, noting that although our study is consistent with their work in terms of the existence of lattice oxygen vacancies as well as the adsorbates evolution at these sites, the effect we proposed could be a further improvement in the catalytic activity of the OER.

SUMMARY

We studied the OER mechanism on $CaMnO_3$ through a thermodynamic approach. The predicted required OER overpotential is close to the experimental value. Our results show that the enhanced activity of lattice oxygen caused by the formation of Mn vacancies on the surface could reduce the energy difference between *OOH and *OH, which may lower the OER overpotential and increase the OER catalytic activity. Therefore, we suggest that doping perovskite-type materials with soluble metal elements to induce metal ion vacancies on the surface in an aqueous environment could enhance their catalytic activity for the OER process.

AUTHOR INFORMATION

Corresponding Author

*E-mail for A.M.R.: rappe@sas.upenn.edu.

ORCID

Tian Qiu: 0000-0001-8510-894X
Diomedes Saldana-Greco: 0000-0002-9861-8751
Andrew M. Rappe: 0000-0003-4620-6496

Notes

The authors declare no competing financial interest.

ACKNOWLEDGMENTS

T.Q. was supported by the Department of Energy Office of Basic Energy Sciences, under grant number DE-FG02-07ER15920. B.T. was supported by the National Natural Science Foundation of China, under grant number 51502219. D.S.-G. was supported by the National Science Foundation, under grant number DMR-1719353. A.M.R. was supported by the Office of Naval Research, under grant number N00014-17-1-2574. The authors acknowledge computational support from the High-Performance Computing Modernization Office of the U.S. Department of Defense, as well as the National Energy Research Scientific Computing center.

REFERENCES

(1) Rossmeisl, J.; Qu, Z. W.; Zhu, H.; Kroes, G. J.; Nørskov, J. K. *J. Electroanal. Chem.* **2007**, *607*, 83−89.
(2) Youngblood, W. J.; Lee, S.-H. A.; Kobayashi, Y.; Hernandez-Pagan, E. A.; Hoertz, P. G.; Moore, T. A.; Moore, A. L.; Gust, D.; Mallouk, T. E. *J. Am. Chem. Soc.* **2009**, *131*, 926−927.
(3) Lee, Y.; Suntivich, J.; May, K. J.; Perry, E. E.; Shao-Horn, Y. *J. Phys. Chem. Lett.* **2012**, *3*, 399−404.
(4) Dismukes, G. C.; Brimblecombe, R.; Felton, G. A. N.; Pryadun, R. S.; Sheats, J. E.; Spiccia, L.; Swiegers, G. F. *Acc. Chem. Res.* **2009**, *42*, 1935−1943.
(5) Su, H. Y.; Gorlin, Y.; Man, I. C.; Calle-Vallejo, F.; Nørskov, J. K.; Jaramillo, T. F.; Rossmeisl, J. *Phys. Chem. Chem. Phys.* **2012**, *14*, 14010−14022.
(6) Du, J.; Zhang, T.; Cheng, F.; Chu, W.; Wu, Z.; Chen, J. *Inorg. Chem.* **2014**, *53*, 9106−9114.
(7) Kim, J.; Yin, X.; Tsao, K.-C.; Fang, S.; Yang, H. *J. Am. Chem. Soc.* **2014**, *136*, 14646−14649.
(8) Rong, X.; Parolin, J.; Kolpak, A. M. *ACS Catal.* **2016**, *6*, 1153−1158.
(9) Man, I. C.; Su, H.-Y.; Calle-Vallejo, F.; Hansen, H. A.; Martínez, J. I.; Inoglu, N. G.; Kitchin, J.; Jaramillo, T. F.; Nørskov, J. K.; Rossmeisl, J. *ChemCatChem* **2011**, *3*, 1159−1165.
(10) Martirez, J. M. P.; Kim, S.; Morales, E. H.; Diroll, B. T.; Cargnello, M.; Gordon, T. R.; Murray, C. B.; Bonnell, D. A.; Rappe, A. M. *J. Am. Chem. Soc.* **2015**, *137*, 2939−2947.
(11) Rong, X.; Kolpak, A. M. *J. Phys. Chem. Lett.* **2015**, *6*, 1785−1789.
(12) Friebel, D.; Louie, M. W.; Bajdich, M.; Sanwald, K. E.; Cai, Y.; Wise, A. M.; Cheng, M.-J.; Sokaras, D.; Weng, T.-C.; Alonso-Mori, R.; Davis, R. C.; Bargar, J. R.; Nørskov, J. K.; Nilsson, A.; Bell, A. T. *J. Am. Chem. Soc.* **2015**, *137*, 1305−1313.
(13) Lee, J. G.; Hwang, J.; Hwang, H. J.; Jeon, O. S.; Jang, J.; Kwon, O.; Lee, Y.; Han, B.; Shul, Y.-G. *J. Am. Chem. Soc.* **2016**, *138*, 3541−3547.
(14) Burke, M. S.; Enman, L. J.; Batchellor, A. S.; Zou, S.; Boettcher, S. W. *Chem. Mater.* **2015**, *27*, 7549−7558.
(15) Gerken, J. B.; McAlpin, J. G.; Chen, J. Y. C.; Rigsby, M. L.; Casey, W. H.; Britt, R. D.; Stahl, S. S. *J. Am. Chem. Soc.* **2011**, *133*, 14431−14442.
(16) Kolpak, A. M.; Li, D.; Shao, R.; Rappe, A. M.; Bonnell, D. A. *Phys. Rev. Lett.* **2008**, *101*, 036102.
(17) Perdew, J.; Ruzsinszky, A.; Gábor, C.; Vydrov, O.; Scuseria, G.; Constantin, L.; Zhou, X.; Burke, K. *Phys. Rev. Lett.* **2008**, *100*, 136406.
(18) Giannozzi, P.; Baroni, S.; Bonini, N.; Calandra, M.; Car, R.; Cavazzoni, C.; Ceresoli, D.; Chiarotti, G. L.; Cococcioni, M.; Dabo, I.; Corso, A. D.; de Gironcoli, S.; Fabris, S.; Fratesi, G.; Gebauer, R.; Gerstmann, U.; Gougoussis, C.; Kokalj, A.; Lazzeri, M.; Martin-Samos, L.; Marzari, N.; Mauri, F.; Mazzarello, R.; Paolini, S.; Pasquarello, A.; Paulatto, L.; Sbraccia, C.; Scandolo, S.; Sclauzero, G.; Seitsonen, A. P.;

DOI: 10.1021/acscatal.7b03987
ACS Catal. 2018, 8, 2218−2224

Smogunov, A.; Umari, P.; Wentzcovitch, R. M. *J. Phys.: Condens. Matter* **2009**, *21*, 395502.
(19) Rappe, A. M.; Rabe, K. M.; Kaxiras, E.; Joannopoulos, J. D. *Phys. Rev. B: Condens. Matter Mater. Phys.* **1990**, *41*, 1227−1230.
(20) Ramer, N. J.; Rappe, A. M. *Phys. Rev. B: Condens. Matter Mater. Phys.* **1999**, *59*, 12471−12478.
(21) http://opium.sourceforge.net.
(22) Louie, S. G.; Froyen, S.; Cohen, M. L. *Phys. Rev. B: Condens. Matter Mater. Phys.* **1982**, *26*, 1738−1742.
(23) Fuchs, M.; Scheffler, M. *Comput. Phys. Commun.* **1999**, *119*, 67−98.
(24) Porezag, D.; Pederson, M. R.; Liu, A. Y. *Phys. Rev. B: Condens. Matter Mater. Phys.* **1999**, *60*, 14132−9.
(25) Himmetoglu, B.; Wentzcovitch, R. M.; Cococcioni, M. *Phys. Rev. B: Condens. Matter Mater. Phys.* **2011**, *84*, 115108.
(26) Lim, J. S.; Saldana-Greco, D.; Rappe, A. M. *Phys. Rev. B: Condens. Matter Mater. Phys.* **2016**, *94*, 165151.
(27) Cococcioni, M.; de Gironcoli, S. *Phys. Rev. B: Condens. Matter Mater. Phys.* **2005**, *71*, 035105.
(28) Monkhorst, H. J.; Pack, J. D. *Phys. Rev. B* **1976**, *13*, 5188−5192.
(29) Bengtsson, L. *Phys. Rev. B: Condens. Matter Mater. Phys.* **1999**, *59*, 12301−4.
(30) Grimaud, A.; Diaz-Morales, O.; Han, B.; Hong, W. T.; Lee, Y.-L.; Giordano, L.; Stoerzinger, K. A.; Koper, M. T. M.; Shao-Horn, Y. *Nat. Chem.* **2017**, *9*, 457.
(31) Zhu, Y.; Zhou, W.; Yu, J.; Chen, Y.; Liu, M.; Shao, Z. *Chem. Mater.* **2016**, *28*, 1691−1697.

DOI: 10.1021/acscatal.7b03987
ACS Catal. 2018, 8, 2218−2224